JACS
JOURNAL OF THE AMERICAN CHEMICAL SOCIETY
Article
pubs.acs.org/JACS

π-Conjugation in $Gd_{13}Fe_{10}C_{13}$ and Its Oxycarbide: Unexpected Connections between Complex Carbides and Simple Organic Molecules

Amelia B. Hadler,[†] Vincent J. Yannello,[†] Wenli Bi,[‡] E. Ercan Alp,[‡] and Daniel C. Fredrickson*[,†]

[†]Department of Chemistry, University of Wisconsin—Madison, 1101 University Avenue, Madison, Wisconsin 53706, United States
[‡]Advanced Photon Source, Argonne National Laboratory, Argonne, Illinois 60439, United States

Supporting Information

ABSTRACT: Carbometalates are a diverse family of solid state structures formed from transition metal (TM)−carbon polyanionic frameworks whose charges are balanced by rare earth (RE) cations. Remarkable structural features, such as transition metal clusters, are often encountered in these phases, and a pressing challenge is to explain how such features emerge from the competing interaction types (RE−TM, TM−TM, TM−C, etc.) in these systems. In this Article, we describe a joint experimental and theoretical investigation of two compounds, $Gd_{13}Fe_{10}C_{13}$ and its oxycarbide $Gd_{13}Fe_{10}C_{13-x}O_x$ ($x \approx 1$), which add a new dimension to the structural chemistry of carbometalates: π-conjugation through both TM−C and TM−TM multiple bonds. The crystal structures of both compounds are built from layers of Fe-centered Gd prisms stacked along c and surrounded by an Fe−C network, and differ chiefly in the stacking sequence of these layers. The phases' identical local structures have two types of Fe environment: trigonal planar FeC_3 sites and H-shaped Fe_2C_4 sites, with unusually short Fe−Fe and Fe−C bonds. ^{57}Fe Mössbauer spectroscopy and DFT-calibrated Hückel calculations on $Gd_{13}Fe_{10}C_{13}$ build a picture of covalent Fe−C σ bonds and conjugated π systems for which Lewis structures can be drawn. Using the reversed approximation Molecular Orbital approach, we can draw isolobal analogies between the Fe centers of this compound and molecular TM complexes: 18-electron configurations could be achieved through σ and π bonds with 18 electrons/Fe for the FeC_3 site and 18-n (n = 2 for an Fe═Fe double bond) electrons/Fe for the Fe_2C_4 site. In this way, the vision of a unified bonding scheme of carbometalates and organometallics proffered by earlier studies is realized in a visual manner, directly from the 1-electron wave functions of the Hückel model. The bonding analysis predicts that $Gd_{13}Fe_{10}C_{13}$ is one electron/formula unit short of an ideal electron count, explaining the tendency of the system toward a small degree of oxygen substitution. Analogies between the π bonding in $Gd_{13}Fe_{10}C_{13}$ and that of the allyl anion help rationalize the presence of trigonal planar Fe and linear C units in the structure. The isolobal analogy between $Gd_{13}Fe_{10}C_{13}$ and an 18-electron coordination complex is expected to apply to carbometalates as a whole, and will be extended to other examples in our future work.

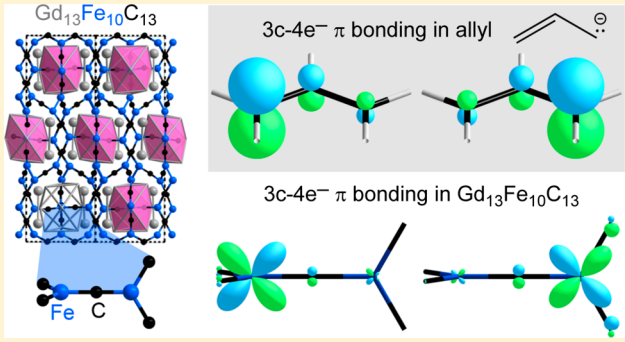

1. INTRODUCTION

A core tenet of materials chemistry is that solid state compounds can exhibit new and exotic structures, bonding, and properties, which could hardly have been expected from the characteristics of their component elements. This promise is vividly realized in ternary carbides, particularly those that involve a transition metal (TM) and rare earth (RE) element. Such phases have increasingly emerged as fascinating materials due to their wide array of crystal structures,[1−12] their magnetic and electronic properties (including superconductivity),[4,5,12−20] and even their reactivity to produce carbon nanotubes.[21] Correlations are also being recognized between these properties and the presence of unusual structural or bonding features, such as C_2^{2-} units[20,22] or Fe clusters,[12,21] which demonstrate the need for an understanding of how bonding and structure are connected in these compounds. In this Article, we work toward this goal through a joint experimental and theoretical analysis of two phases, $Gd_{13}Fe_{10}C_{13}$ and its oxycarbide derivative, which exhibit remarkable dimers of Fe with bond distances as short as 2.36 Å.

Our initial investigations into the Gd−Fe−C system were driven by the conflicts we perceived in the preferred bonding modes of its component binary subsystems, a tension we term *chemical frustration* and consider a source of complexity in ternary compounds.[23,24] While Gd−Fe binaries such as the Laves-type phase $GdFe_2$ are built from dense packings of metal tetrahedra,[25] C prefers to occupy larger holes such as the octahedra of fcc metal lattices, exemplified by the defect NaCl-type interstitial carbide $GdC_{0.33}$.[26−28] We expected that

Received: June 11, 2014
Published: August 5, 2014

   dx.doi.org/10.1021/ja505868w | J. Am. Chem. Soc. 2014, 136, 12073−12084

combining these three elements would lead to chemical frustration in the form of competition between the geometrical preferences of metal−metal and metal−carbon interactions. In $Gd_{13}Fe_{10}C_{13}$ and its oxycarbide, the result of this frustration is the placement of C atoms into the octahedral holes of a Gd−Fe sublattice similar to the Fe_2P structure.[29] Within this arrangement, networks built from unusually short Fe−C and Fe−Fe contacts arise that are suggestive of interesting bonding interactions.

An approach to analyzing these bonding features is offered by methods developed recently in our group for tracing isolobal analogies between molecular TM complexes and intermetallic phases−analogies that might be expected to apply for carbometalates as well. Beginning with the fluorite-type phase $NiSi_2$ and its complex derivatives $Fe_8Al_{17.4}Si_{7.6}$ and $Co_3Al_4Si_2$, we have found that for a growing number of compounds, density of states (DOS) pseudogaps near the Fermi energy (E_F) can be traced to filled octadecets (18-electron configurations) on the TM atoms.[30,31] The origin of the pseudogaps is the closed-shell nature of the electronic structure when each of the TM atoms' one s, three p, and five d valence orbitals is associated with a filled bonding or nonbonding orbital. Driven by this observation, we developed a theoretical approach to quickly identify such simple local bonding schemes in solid state compounds: the reversed approximation Molecular Orbital (raMO) method.[32]

The idea of applying the 18-electron rule and other organometallic bonding concepts to carbometalates, RE−TM−C phases in which TM−C bonding interactions predominate, is not new. Their structures can often be described in terms of 1-, 2- or 3-dimensional networks of TM−C bonds, which pass through sublattices of RE atoms.[10,33] This suggests a bonding picture in which RE^{3+} cations counterbalance the charge of a TM−C polyanionic network. The local coordination of the TM atoms within these TM−C networks frequently resembles that in a coordination compound, and the carbon atoms are thus sometimes informally treated as C^{4-} anions. In simple cases, stable 18-electron configurations can then be assigned to the TM sites by determining the oxidation of the TM atoms and considering dative TM−C bonding.[8,9,17,18,34−36] However, in more complex carbometalates, such as those containing TM−TM bonding in pairs, chains, or clusters, the situation is much more challenging,[3,11,18,24,37,38] and even in relatively simple carbometalates, such as YCoC, TM−C π interactions add to the richness of the bonding.[39]

Over the course of this Article, we will see that the raMO approach, in conjunction with synthesis, structure determination, and ^{57}Fe Mössbauer spectroscopy, can derive direct links between the electronic structure of carbometalates and molecular bonding schemes. From the wave functions of the complex $Gd_{13}Fe_{10}C_{13}$ structure, we will see the connections between ternary carbides and organometallics envisioned earlier studies remerge,[36,39−42] but this time with the vividness of localizing bonding orbitals drawn for each covalently shared electron pair. A dense network of covalent σ and conjugated π bonds will be uncovered which offers a unique view into how Fe can use its valence orbitals for bonding, as well as an unexpected analogy to multiple bonding in simple organic molecules.

2. TECHNICAL PROCEDURES

2.1. Synthesis of $Gd_{13}Fe_{10}C_{13}$ and $Gd_{13}Fe_{10}C_{13-x}O_x$. Several synthetic procedures were developed to obtain single crystals of both phases, to synthesize $Gd_{13}Fe_{10}C_{13}$ while excluding $Gd_{13}Fe_{10}C_{13-x}O_x$, and to introduce oxygen for $Gd_{13}Fe_{10}C_{13-x}O_x$ formation in a controlled fashion. For the initial synthesis, the pure elements (gadolinium, Strem Chemicals, 99.9% REO, ingot, filed; iron, Strem Chemicals, 99.9% metals basis, powder 1−9 μm, used as received; carbon, Strem Chemicals, 99.999%, powder −200 mesh, used as received) were weighed out in a 1:1:1 ratio, mixed, and pressed into pellets in an Ar-filled glovebox. The resulting pellets were arc-melted three times to achieve maximal homogeneity. The pellets were removed from the glovebox without (as we will see is important below) special precautions taken to exclude air exposure before they were sealed in evacuated fused silica tubing. Sealed samples were annealed at 900 °C for 350−400 h in a muffle furnace, then quenched in an ice−water bath.

For all other syntheses, filings from a high-purity Gd ingot (Ames Laboratory, 99.99% metals basis) were used as a Gd source to minimize the effects of the oxide impurities commonly found in commercial Gd.[43] To synthesize $Gd_{13}Fe_{10}C_{13}$ and exclude $Gd_{13}Fe_{10}C_{13-x}O_x$, Gd, Fe, and C were weighed out in a ratio of 13:10:13, pressed into pellets, and arc-melted in an Ar-filled glovebox. The resulting pellets were wrapped in Ta foil, transferred from the glovebox to a vacuum line in an Ar-filled silica tube equipped with a stopcock to prevent exposure to air, and then sealed under vacuum in this tube for annealing. Syntheses with the goal of intentional incorporation of oxygen into $Gd_{13}Fe_{10}C_{13-x}O_x$ were performed using either Gd_2O_3 as a starting material or the introduction of ultrahigh purity O_2 in a controlled environment prior to annealing (see Supporting Information for more details). In all cases, the sealed samples were annealed at 900 °C for 350 h, then quenched in ice water.

2.2. Phase Analysis with Powder X-ray Diffraction. Due to the presence of an air-sensitive impurity (see Supporting Information), reaction containers were opened and handled in a N_2-filled glovebox. The reaction products were shiny gray ingots, which were brittle and easily crushed. The crushed samples were ground and packed into 0.1 or 0.3 mm diameter borosilicate glass capillaries that were then trimmed to size and sealed with epoxy.

For preliminary phase analysis, powder X-ray diffraction data was collected on a Rigaku Rapid II X-ray diffractometer with Mo Kα radiation (λ = 0.709319 Å). Data was collected on the area detector using a 15 min exposure time and converted to $2\theta - I$ data using Rigaku's 2DP program. For higher-resolution powder diffraction data, measurements were taken on the synchrotron beamline 11-BM at the Advanced Photon Source, Argonne National Laboratory, using an average wavelength of 0.413219 Å (see Supporting Information). The resulting powder patterns were compared to calculated patterns for the title phases. Most samples contained either $Gd_{13}Fe_{10}C_{13}$ alone or a mixture of $Gd_{13}Fe_{10}C_{13}$ and $Gd_{13}Fe_{10}C_{13-x}O_x$ as major phases; see Supporting Information for analysis of impurities.

2.3. Single Crystal X-ray Diffraction Measurements for $Gd_{13}Fe_{10}C_{13-x}O_x$. The data collection procedures for the single crystals of $Gd_{13}Fe_{10}C_{13}$ were described in our earlier communication,[24] so we focus here on experiments for $Gd_{13}Fe_{10}C_{13-x}O_x$. Full data sets on 8 crystals of $Gd_{13}Fe_{10}C_{13-x}O_x$ were collected using our lab's Agilent Xcalibur E diffractometer or an Agilent SuperNova A diffractometer. For the data set discussed in detail here, an irregularly shaped single crystal was picked from a crushed sample (that had been exposed to UHP O_2) and mounted in air, with no observable signs of oxidation. X-ray diffraction measurements were performed on an Agilent SuperNova A diffractometer with a Mo Kα sealed-tube X-ray source (λ = 0.71069 Å). Frame data was processed using the program CrysalisPro Ver. 171.36.24.[44] Further details on the selected crystal are given in Table 1.

2.4. Structure Solution and Refinement of $Gd_{13}Fe_{10}C_{13-x}O_x$. Examination of the collected intensities with a peak search and unit cell determination yielded a metrically orthorhombic unit cell, with a =

Table 1. Crystal Data for $Gd_{13}Fe_{10}C_{13-x}O_x$[a]

Chemical formula	$Gd_{13}Fe_{10}C_{12.02}O_{0.98}$[b]
Pearson symbol	*oF*288
Space group	*Fdd*2 (No. 43)[c]
a (Å)	9.2299(5)
b (Å)	16.0158(8)
c (Å)	31.6935(14)
Cell volume (Å^3), calc. density (g/cm^3)	4685.1(4), 7.8312
Crystal dimensions (mm)	0.05 × 0.04 × 0.02
Crystal color	Metallic gray
Data collection temperature	Room temperature
Radiation source, λ (Å)	Mo K_α, 0.7107
Absorption coefficient (mm^{-1})	42.171
Absorption correction	Multiscan and spherical
θ_{min}, θ_{max}	3.2, 29.47
Number of reflections	6437
R_{int} ($I > 3\sigma$, all)	3.01, 3.04
Unique reflections ($I > 3\sigma$, all)	2403, 2616
Number of parameters	129
R ($I > 3\sigma$), R_w ($I > 3\sigma$)	2.43, 5.07
R(all), R_w (all)	2.74, 5.23
S ($I > 3\sigma$), S(all)	1.06, 1.07
$\Delta\rho_{max}$, $\Delta\rho_{min}$ (electrons/Å^3)	1.47, −1.04
Flack parameter	0.02(4)

[a]A crystallographic information file containing further details can be obtained from the Fachinformationszentrum Karlsruhe (E-mail: crysdata@fiz-karlsruhe.de), on quoting the depository number 424138. [b]See text for procedures for oxygen refinement. [c]The nonstandard setting *F*2*dd* was used for consistency of the *a*, *b*, and *c* directions with those of the trigonal $Gd_{13}Fe_{10}C_{13}$ phase.

9.2299(5) Å, *b* = 16.0158(8) Å, and *c* = 31.6935(14) Å, which indexed 3875 of the 6167 peaks (62.8%). Examination of reciprocal lattice reconstructions yielded systematic absences consistent with the *F*2*dd* setting of the space group *Fdd*2 (no. 43). Subsequent refinement supported this assignment.

An initial structural solution was obtained using the charge-flipping algorithm[45,46] in the program *SUPERFLIP*,[47] which yielded atomic positions and assignments for all Gd and Fe sites. These site assignments were confirmed by refinement on F^2 with the program *JANA2006*.[48] An examination of the Fourier difference map yielded atomic positions for C/O atoms. Isotropic refinement of the carbon sites led to a wide distribution of U_{iso} values, with one site (C/O5) persistently showing a value close to zero, suggesting that the site may be occupied by a slightly heavier element such as oxygen. In testing all of the C sites, the C/O5 and C/O7 sites showed oxygen content of 25(6)% and 24(6)%, respectively; no other sites demonstrated partial oxygen content.

We were initially doubtful about the ability of our diffraction data to discern such subtle differences in scattering factors; however, several recent papers have reported success with such refinements.[49−51] Further support for these assignments came from comparing refinements on data sets for several crystals, which show similar patterns of likely oxygen incorporation on the C/O5 site as well as the C/O7 site. Every data set consistently showed the C/O5 site exhibiting positive occupancies for O. The C/O7 site could be refined as mixed with some amount of oxygen, although for some crystals this amount was less than the uncertainty in the occupancy. No other sites could consistently be refined with partial oxygen content. Refined compositions for all crystals ranged from $Gd_{13}Fe_{10}C_{11.2(3)}O_{1.8(3)}$ to $Gd_{13}Fe_{10}C_{12.37(15)}O_{0.63(15)}$. The discrepancy in occupancies between these crystals and the reported crystal, as well as the large uncertainties for C/O occupancies, suggest that the composition of $Gd_{13}Fe_{10}C_{13-x}O_x$ as determined by single crystal X-ray diffraction should be regarded only as an approximation, as is consistent with general crystallographic experience.

Due to the highly absorbing nature of this crystal, individual carbon atomic displacement parameters were restrained to be equal during the final refinement. With Gd and Fe sites refined anisotropically, the composition of the phase refined to $Gd_{13}Fe_{10}C_{12.02(12)}O_{0.98(12)}$, leading to $R[I > 3\sigma(I)] = 2.43$. Since the space group *Fdd*2 is noncentrosymmetric, an inversion twin (Flack parameter) was refined; this supported the absolute configuration of the model but did not affect the refined model.[52] Refined atomic coordinates and atomic displacement parameters are given in the Supporting Information (Table S1), along with selected interatomic distances (Table S2). All interatomic distances are consistent with the atomic identities assigned to the sites (see Supporting Information).

2.5. Elemental Analysis Using Energy Dispersive X-ray Spectroscopy. For semiquantitative determination of elemental compositions, pieces of crushed samples containing a mixture of $Gd_{13}Fe_{10}C_{13}$ and $Gd_{13}Fe_{10}C_{13-x}O_x$ were suspended in epoxy doped with graphite powder. The samples were hand-polished against silicon carbide papers, and polished further with a 1-μm diamond solution on a diamond wheel. The polished samples were then examined with a Hitachi S-3100N scanning electron microscope fitted with an EDS probe (voltage: 15 kV). The phases of interest could not be distinguished from one another due to their similar compositions and to the difficulty in distinguishing carbon from oxygen with EDS. This phase mixture provided an average composition of $Gd_{14.9(3)}Fe_{10}$. No other elements heavier than sodium were observed. Significant carbon and minor oxygen content was seen but not quantified due to the limitations of EDS with light elements. Additional impurity phases were also observed, chiefly an oxygen-rich phase. All samples showed slight surface oxidation.

2.6. Mössbauer Spectroscopy Analysis of $Gd_{13}Fe_{10}C_{13}$. Samples that showed $Gd_{13}Fe_{10}C_{13}$ as the majority phase were ground to powders in air and used for Mössbauer spectroscopy. The Mössbauer transition spectra were recorded using a constant acceleration drive. The spectrometer was calibrated using an iron foil. The ^{57}Co source used was a point source with 0.4 mm diameter, and the relative activity was 3 mCi. A VORTEX detector with 150 eV resolution was used to discriminate the 14.4 keV radiation. Typical spectra were collected over several days at room temperature, over a range of ±8 mm/s. Data analysis was performed using in-house software.

2.7. Electronic Structure Calculations. The band energies and electronic density of states distribution of $Gd_{13}Fe_{10}C_{13}$, as well as the DFT-calibrated Hückel parameters[53] needed for the reversed approximation Molecular Orbital (raMO) analysis, were taken from our previous theoretical work on this phase.[24] Hückel parameters refined earlier for benzene were used for raMO analysis on the allyl anion.[32] See the Supporting Information for tables of these parameters.

Since the wave functions at Γ are used for the raMO analysis, a 2 × 2 × 1 supercell of $Gd_{13}Fe_{10}C_{13}$ was used to map several special k-points of the primitive cell to the Γ point. A Hückel calculation using the DFT-calibrated parameters was carried out on this supercell using YAeHMOP.[54] The Hamiltonian matrix for the Γ point was printed and imported into Matlab for raMO analysis. Crystal orbital Hamilton populations[55] were also generated using YAeHMOP. Projected density of states curves were calculated for Fe−Fe π and π^* raMOs in Matlab using the wave functions at the Γ point for the supercell.

3. RESULTS AND DISCUSSION

3.1. Synthesis of $Gd_{13}Fe_{10}C_{13}$ and $Gd_{13}Fe_{10}C_{13-x}O_x$. Our original synthetic target in the Gd−Fe−C ternary system was the phase GdFeC, which had been reported by Stadelmaier et al., but whose crystal structure remained undetermined.[56] After annealing at 900 °C for 400 h, a sample with the composition GdFeC yielded a mixture of two phases for which we found single crystals: a trigonal phase which crystallized in the space group $P3_121$ with cell parameters *a* = 9.247(3) Å and *c* = 23.713(8) Å; and an orthorhombic phase, crystallizing with the symmetry *Fdd*2 with *a* = 9.2299(5) Å, *b* = 16.0158(8) Å, and *c*

dx.doi.org/10.1021/ja505868w | J. Am. Chem. Soc. 2014, 136, 12073−12084

= 31.6935(14) Å (*F2dd* setting, to simplify comparison with the trigonal phase).

Both phases had the same refined composition of $Gd_{13}Fe_{10}C_{13}$, which raised the question of their relationship to each other. One possibility was that they might be polymorphs whose relative stabilities could be affected by temperature or composition. However, the observed ratios of the two phases could not be correlated with changes in the annealing temperature or nominal composition.

Clues to the factors distinguishing these phases appeared when we analyzed the refined structure model of the orthorhombic $Gd_{13}Fe_{10}C_{13}$ phase in detail. We observed that the negative U_{iso} value of one carbon site became positive when modeled as a mixed carbon/oxygen site, and we later found that the physical realism of the atomic displacement parameters in the model was improved when a second site was allowed a significant degree of oxygen substitution. Refined oxygen content varied from crystal to crystal, but the same two sites were seen to incorporate oxygen, and crystals of that phase could consistently be refined with the composition $Gd_{13}Fe_{10}C_{13-x}O_x$, with x varying from 0.6 to 1.8.

The possibility of oxygen incorporation into the samples ultimately led us to trace the emergence of the orthorhombic phase to two different aspects of our synthetic procedure: brief exposure of the arc-melted sample to air before sealing in fused silica for annealing, and oxygen impurities present in the commercial Gd used in our syntheses. When we used high-purity Gd in the syntheses and carefully prevented exposure of the sample to air, we obtained $Gd_{13}Fe_{10}C_{13}$ as the major phase, with little or no detectable $Gd_{13}Fe_{10}C_{13-x}O_x$ present.

To confirm the presence of oxygen in $Gd_{13}Fe_{10}C_{13-x}O_x$, the phase was synthesized in a controlled fashion, in which our arc-melted pellets were exposed to high-purity O_2 at a pressure of 160 Torr (the partial pressure of O_2 in air) prior to annealing. Figure 1 shows a synchrotron powder pattern of one of the O_2-exposed samples, compared with a control sample. $Gd_{13}Fe_{10}C_{13}$ is the clear majority phase in the unexposed sample, while a few minor peaks could signify that a very small amount of $Gd_{13}Fe_{10}C_{13-x}O_x$ is also present. However, in the sample exposed to O_2 for 60 min, a significantly larger amount of $Gd_{13}Fe_{10}C_{13-x}O_x$ appears alongside the expected $Gd_{13}Fe_{10}C_{13}$ content, suggesting that the amount of $Gd_{13}Fe_{10}C_{13-x}O_x$ in a sample is related to O_2 exposure.

This reactivity toward oxygen, however, is not necessarily an intrinsic property of the original $Gd_{13}Fe_{10}C_{13}$ phase, especially as crystals of this compound appear to be stable in air. The oxygen likely reacts instead with metastable secondary phases that are present in the arc-melted sample before it is annealed. Also, with the use of gadolinium as a starting material, we cannot rule out a role for impurities to catalytically enhance the reactivity of the samples toward oxygen.

The results of a second experiment, in which a sample was prepared with Gd_2O_3 as a starting material gave similar results in terms of the formation of $Gd_{13}Fe_{10}C_{13-x}O_x$ alongside $Gd_{13}Fe_{10}C_{13}$, as is presented in Figure S3 of the Supporting Information. Both experiments suggest that oxygen incorporation is the source of the orthorhombic phase and support its designation as an oxycarbide.

3.2. Crystal Structures of $Gd_{13}Fe_{10}C_{13}$ and $Gd_{13}Fe_{10}C_{13-x}O_x$. Their similar compositions suggest that the crystal structures of $Gd_{13}Fe_{10}C_{13-x}O_x$ and $Gd_{13}Fe_{10}C_{13}$ are closely related, a view reinforced by their related unit cell parameters. The cell parameters of $Gd_{13}Fe_{10}C_{13-x}O_x$ can be

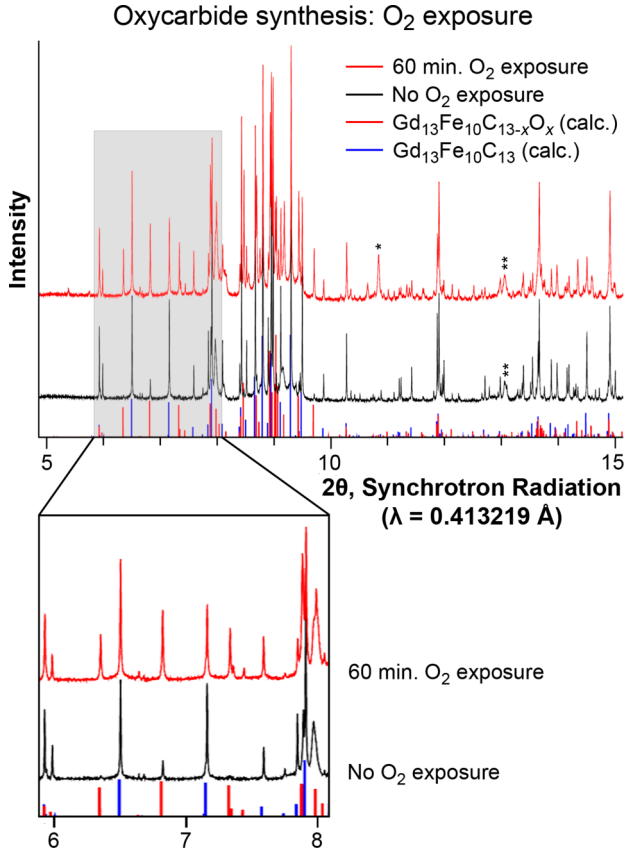

Figure 1. Synchrotron powder X-ray diffraction patterns for samples with composition $Gd_{13}Fe_{10}C_{13}$. The sample shown in black was not exposed to O_2, while the sample shown in red was exposed to ultra high purity O_2 for 60 min. The inset region shows the growth of $Gd_{13}Fe_{10}C_{13-x}O_x$ (calculated pattern shown in red) at the expense of $Gd_{13}Fe_{10}C_{13}$ (blue) after O_2 exposure. Impurities: * $-GdFe_3$; ** $-Gd_3C$.

interpreted as an orthorhombic setting of a metrically hexagonal unit cell with $a = b = 9.248$ Å and $c = 31.734$ Å, which has similar basal dimensions to those of the trigonal $Gd_{13}Fe_{10}C_{13}$ ($a = b = 9.247$ Å and $c = 23.713$ Å). An examination of their crystal structures quickly makes clear the expected structural link (Figure 2): both structures are based on layers of Fe-centered Gd tricapped trigonal prisms (TTPs), which are stacked along c. They differ in the number of layers per unit cell, with $Gd_{13}Fe_{10}C_{13}$ containing three layers of prisms (colored by layer height) and $Gd_{13}Fe_{10}C_{13-x}O_x$ containing four. This accounts for the c parameter of $Gd_{13}Fe_{10}C_{13-x}O_x$ being approximately 4/3 that of $Gd_{13}Fe_{10}C_{13}$.

Looking at a single layer (Figure 2e,f) reveals that on a local level, the two phases have the same basic hexagonal layer structure, which explains their similar a and b side lengths. This basic layer, shown from above in Figure 3a, is built from Fe-centered Gd TTPs and Gd dumbbells, which recall the common Fe_2P structure type.[29]

In both phases, these TTPs are interpenetrated by an Fe−C network that grows outward from the central Fe atom of the prism. This network surrounds the prism layers and prevents them from fusing through shared faces along c, causing the formation of the layered structures of both phases (Figure 3b). A closer look at these networks reveals two distinct types of Fe environment. Four of the six crystallographic Fe sites in each phase center Gd TTPs and are bound in trigonal planar fashion

dx.doi.org/10.1021/ja505868w | J. Am. Chem. Soc. 2014, 136, 12073−12084

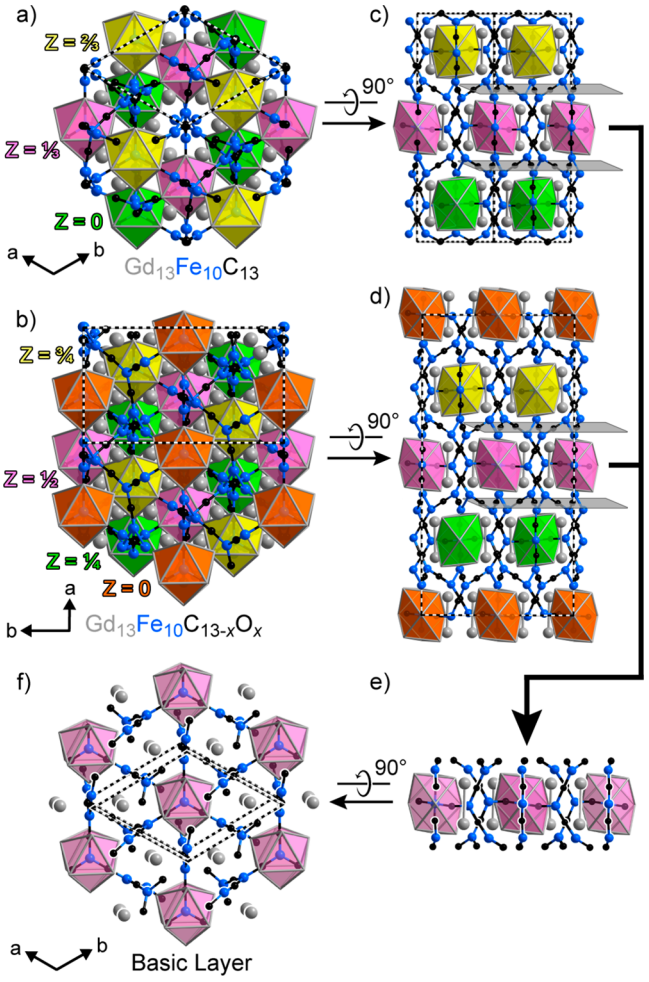

Figure 2. Crystal structures of $Gd_{13}Fe_{10}C_{13}$ and $Gd_{13}Fe_{10}C_{13-x}O_x$. Both structures are built from (a and b) layers of Gd-centered tricapped trigonal prisms (colored by layer height), shown here down *c*. Rotating the structures reveals that (c) $Gd_{13}Fe_{10}C_{13}$ is built from three prism layers, while (d) $Gd_{13}Fe_{10}C_{13-x}O_x$ is built from four. When one layer is (e) removed from each structure and (f) rotated, the same hexagonal basic layer structure appears for both phases.

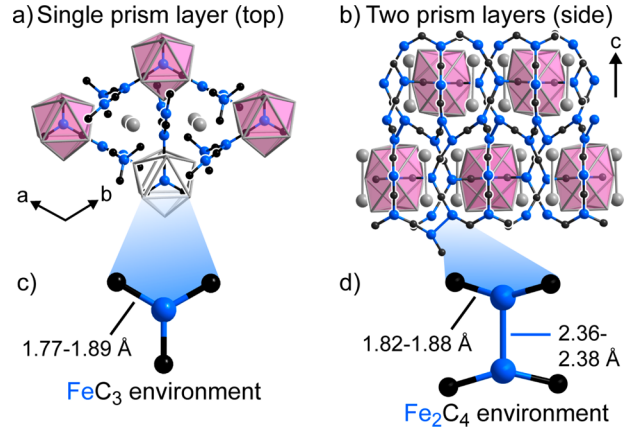

Figure 3. Local structural features of $Gd_{13}Fe_{10}C_{13}$ and $Gd_{13}Fe_{10}C_{13-x}O_x$. (a) A single prism layer viewed down *c* contains Gd TTPs and Gd dumbbells. (b) An Fe−C network surrounds the TTPs, preventing two prism layers from stacking directly. (c) Four out of six Fe sites are bound in trigonal planar fashion to C atoms, forming an FeC_3 fragment. (d) Two out of six Fe sites can be found in Fe_2C_4 fragments.

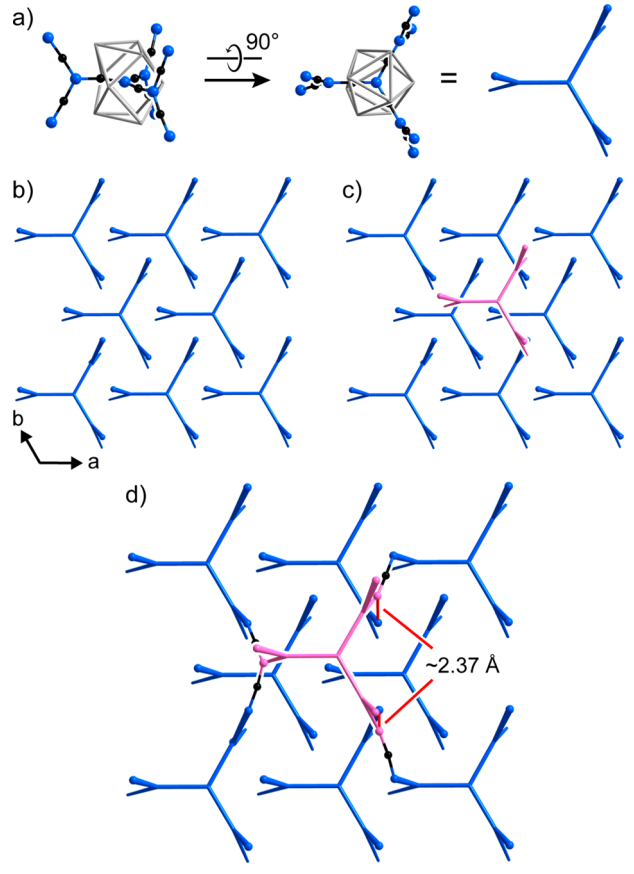

Figure 4. Architecture of Fe−C networks in $Gd_{13}Fe_{10}C_{13}$ and $Gd_{13}Fe_{10}C_{13-x}O_x$. (a) The recurring $Fe_{10}C_9$ paddle wheel fragment centered on the Gd TTPs. (b) These fragments pack hexagonally in a single prism layer. (c) Alignment of paddle wheels between layers, and (d) their linkages through bridging C atoms (black) and close Fe−Fe contacts (red).

to three C atoms (Figure 3c). The other two crystallographic Fe sites form H-shaped units shown in Figure 3d, in which they are bound to one additional Fe and two C atoms to form a unit with composition Fe_2C_4.

By joining these two types of Fe environments through shared C atoms, we can trace how the Fe−C network connects different prism layers. Figure 4a shows a larger cluster within this network which is formed from the FeC_3 site which centers each TTP. Each C atom in an FeC_3 environment is part of an additional FeC_3 unit perpendicular to the first, creating a fragment shaped like a three-fold paddle wheel. The six new C atoms are themselves bound to an additional Fe to create $Fe_{10}C_9$ paddle wheels (Figure 4a) similar to the Pt_7Si_3 units of $Ca_{10}Pt_7Si_3$.[57] This fragment can be used as a building block for the full Fe−C framework in the structure, which is made easier when we move to a simplified cylinder representation based on the positions of the Fe atoms (Figure 4a, far right).

Figure 4b shows one layer of $Fe_{10}C_9$ paddle wheels, viewed down *c*. These units, like the TTPs they center, pack in a hexagonal array without any intralayer bonding. Instead, each paddle wheel connects to other paddle wheels in the layers above and below it, as is shown in Figures 4c and d. One fragment (pink) from the layer directly above the blue layer is added in Figure 4c, and the connections between this pink fragment and the blue fragments below are drawn out in Figure

dx.doi.org/10.1021/ja505868w | J. Am. Chem. Soc. 2014, 136, 12073−12084

4d. The pink unit makes four connections to the adjacent blue layer through shared C atoms. However, two of the Fe atoms in the pink fragment are too close to neighboring Fe atoms in the layer below to allow for a bridging C atom. These close connections, shown in red, form the Fe−Fe bonds which center the H-shaped Fe_2C_4 units shown in Figure 3d. Fe−Fe bonds are thus only found as connections between prism layers.

The Fe−C and Fe−Fe distances that emerge from this network hint at the presence of rich bonding interactions which are difficult to reconcile with the view of the C atoms behaving as simple C^{4-} anions. Our previous communication described the short Fe−Fe contacts in the Fe_2C_4 units of $Gd_{13}Fe_{10}C_{13}$, and explained the Fe−Fe distances of 2.36−2.38 Å[24] (versus 2.64 Å for the sum of the covalent radii of two Fe atoms)[58] in terms of multiple bond character. The corresponding contacts in $Gd_{13}Fe_{10}C_{13-x}O_x$ are nearly identical, with Fe−Fe distances of 2.37 Å, and a similar bonding picture is expected to apply to this phase as well.

The Fe−C distances in both phases are also unexpectedly short. In $Gd_{13}Fe_{10}C_{13}$ and $Gd_{13}Fe_{10}C_{13-x}O_x$, Fe−C bond distances range from 1.77 to 1.89 Å, compared to 2.01 Å for the sum of the covalent radii of Fe and C, and fall on the lower end of the distribution of observed Fe−C distances in binary carbides (1.84 to 2.42 Å). A useful comparison (following in the footsteps of King)[36] is to the organometallic complex $Fe(CO)_5$, whose Fe−C distances of 1.754−1.805 Å[59] are associated with π back-donation. We may anticipate that the similarly short distances in $Gd_{13}Fe_{10}C_{13}$ and $Gd_{13}Fe_{10}C_{13-x}O_x$ also reflect substantial π interactions.

3.3. Mössbauer Spectroscopic Analysis of $Gd_{13}Fe_{10}C_{13}$. As we described in the last section, the Fe−C and Fe−Fe distances in $Gd_{13}Fe_{10}C_{13}$ and its oxycarbide are suggestive of more covalent bonding than would be expected from a strictly ionic model of this compound. Important clues into the bonding of this phase were obtained earlier through magnetic property measurements. These measurements revealed that $Gd_{13}Fe_{10}C_{13}$ orders ferromagnetically below ~55 K, and the magnitude of its magnetic moment at 6 K is consistent with that of Gd^{3+} cations. These results suggested that magnetic behavior in $Gd_{13}Fe_{10}C_{13}$ could reasonably be attributed to the Gd sublattice alone, with little contribution from the Fe sites.[24]

To gain deeper insight into the local electronic structure of the Fe atoms, we turned to ^{57}Fe Mössbauer spectroscopy. Mössbauer spectra were measured on a nearly phase-pure sample of $Gd_{13}Fe_{10}C_{13}$ (small amounts of Gd_3C were the only impurity seen via powder X-ray diffraction) at room temperature. Figure 5 shows the resulting spectrum (spectra of three additional samples, as well as spectral parameters for all samples, can be found in the Supporting Information). Two peaks of roughly equal size are apparent at −1.00 and 0.51 mm/s. Due to their large peak widths, these features are best fit to a set of overlapping doublets (their sum is shown in gray) with isomer shifts of δ = −0.261(6) and −0.235(6) mm/s and quadrupole splittings of Δ = 1.69(3) and 1.43(3) mm/s, respectively. The ratios between the two doublets vary from sample to sample, suggesting that the high degree of overlap between the doublets makes quantitative analysis difficult. The overlap is too large to assign a specific Fe environment to each doublet, but the absence of additional signals affirms that there are no detectable Fe-containing impurities in this sample.

Quadrupole splitting arises from deviations from cubic symmetry around an Fe site.[60] The large quadrupole splitting

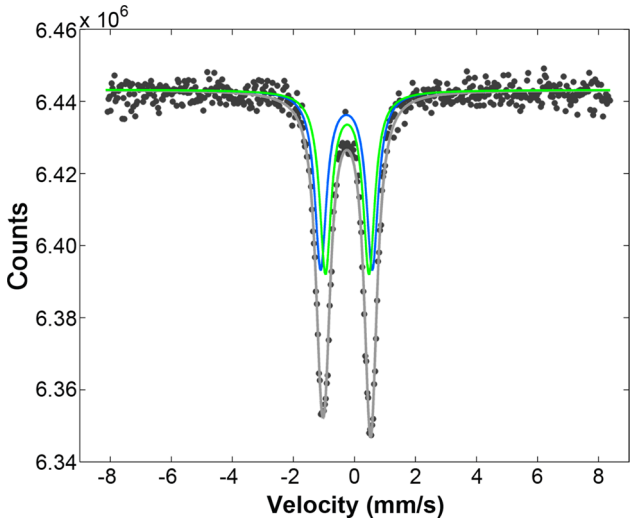

Figure 5. Mössbauer spectrum of $Gd_{13}Fe_{10}C_{13}$ at 298 K. The fit for Site 1 is outlined in blue, while the fit for Site 2 is traced in green. The summation of the two sites is shown in gray.

values seen for both Fe environments can then be understood to reflect the low site symmetry for all Fe atoms in the phase. As seen in Figure 3, both Fe environments have approximate local symmetries significantly lower than cubic: D_{3h} for the FeC_3 sites and C_2 for the Fe_2C_4 sites.

The isomer shifts provide a window into the charge density on the Fe atoms by probing the s electron density at the nucleus, and thus offer information about the oxidation state and bond polarity.[60] However, isomer shifts are not simple functions of charge, so it is important to calibrate ourselves against spectra of related Fe-containing phases. A ^{57}Fe Mössbauer study on simple Fe binary intermetallics found that Fe-main group binary compounds universally showed positive isomer shifts, while binaries of Fe with early transition metals had negative isomer shifts.[61] Significantly, $GdFe_2$ has an isomer shift of −0.267 mm/s.[62] From these results, we can conclude that, when combined with an electronegative element, the 4s electron population of the Fe is lowered by partial electron transfer from the Fe to the more electronegative element, leading to slightly positive isomer shifts. When Fe is combined with a more electropositive element, its 4s electron population is increased by electron transfer to the Fe, which tends toward negative isomer shifts. For simplicity, we can refer to Fe in intermetallics with more electronegative elements as cationic, while Fe in intermetallics with more electropositive elements is considered anionic.

Both Fe environments for $Gd_{13}Fe_{10}C_{13}$ show significantly negative isomer shifts of −0.26 and −0.24 mm/s, which in this context likely indicate anionic rather than cationic Fe.[63] Given the similarity in isomer shift to $GdFe_2$, it seems likely that the negative isomer shifts for each site arise from electron transfer from the Gd framework around the Fe environments. This role of electron transfer to the Fe is emphasized by comparison to earlier ^{57}Fe Mössbauer studies of Fe-containing ternary or quaternary carbides. Among the spectral features of such carbides, these values are on the negative end of the range of observed isomer shifts (ca. −0.23 to +0.21).[13,64,65]

The nearly identical isomer shifts of the two sites suggest that the two types of Fe have similar amounts of s electron density at the nucleus, and therefore similar charges. In light of these results, the formal charges of Fe^{2+} and $Fe^{0.25+}$ we obtained

earlier when treating C as C^{4-} anions[24] fail to fully capture the electron-rich nature of these Fe atoms. In the next section of this paper, we will use this result as the basis for a revised picture of bonding in $Gd_{13}Fe_{10}C_{13}$ and $Gd_{13}Fe_{10}C_{13-x}O_x$.

3.4. raMO Analysis of $Gd_{13}Fe_{10}C_{13}$: the FeC_3 Units. The ^{57}Fe Mössbauer spectra just described suggest that the simple picture of C^{4-} ligands connected to Fe cations through dative bonds does not encapsulate the entire bonding picture for $Gd_{13}Fe_{10}C_{13}$. How should we adjust our bonding scheme in light of these results? An important clue is found in the density of states (DOS) of this phase (Figure 6). This DOS curve exhibits a deep electronic pseudogap at the Fermi energy (E_F) in the midst of a dense set of states based on Fe 3d orbitals. The presence of such a pseudogap in the DOS of $Gd_{13}Fe_{10}C_{13}$ suggests that the Fe sites in this structure are likely to be stabilized by their achieving favorable electron configurations.

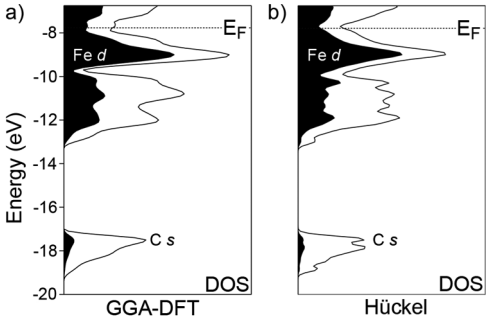

Figure 6. Density of states for $Gd_{13}Fe_{10}C_{13}$ calculated using (a) density functional theory (DFT) and (b) a DFT-calibrated Hückel model. Both curves show a deep pseudogap at the Fermi energy (E_F) in a region dominated by Fe d states. This figure is reproduced from ref 24, with the kind permission of the American Chemical Society. Copyright 2012.

One means of analyzing the ideal electron count that underlies such pseudogaps is the recently developed reversed approximation Molecular Orbital (raMO) analysis.[32] The raMO analysis involves reversing the approach used for typical MO calculations in order to create localized molecular orbitals for a local environment in an intermetallic phase. First, an MO diagram is proposed as a description of the bonding in a fragment of the structure. We then examine how well these orbitals can be reproduced by the occupied crystal orbitals of the intermetallic phase. This is accomplished by solving the Schrödinger equation for the model system (in which the target orbitals are eigenfunctions) in the basis of the fully occupied wave functions of the full crystal structure. The resulting raMO functions provide the best possible approximations to the initial target orbitals, allowing us to examine how well the target orbitals are represented in the true wave functions, and what interactions they are involved in.

In the case of $Gd_{13}Fe_{10}C_{13}$, the features of interest are the two Fe environments shown in Figure 3, panels c and d: the trigonal planar FeC_3 unit and the H-shaped Fe_2C_4 unit. If we follow the earlier proposals that 18-electron configurations are important for the stability of carbometalates, we would expect nine functions sharing the symmetry properties of the nine transition metal s, p, and d valence atomic orbitals to be completely filled for each of the Fe atoms. Our target orbitals are thus the nine Fe s, p, and d orbitals.

We begin our raMO analysis of $Gd_{13}Fe_{10}C_{13}$ with the simpler of the two Fe sites: the FeC_3 site (Figure 7). A raMO analysis using the central Fe atom's s, p, and d atomic orbitals as target functions generates nine functions, one for each of the Fe target orbitals. Each function appears as largely localized to the Fe and its first coordination sphere, and has room for two electrons.

The nine raMO functions can be classified by the orientations of their target orbitals relative to the FeC_3 plane into three σ functions (s, p_x, p_y), three π functions (p_z, d_{xz}, d_{yz}), one nonbonding function (d_{z^2}), and two functions of less certain character (d_{xy}, $d_{x^2-y^2}$). The three σ functions are based on a set of an s orbital and two coplanar p orbitals (Figure 7, top), familiar from the MOs of an sp^2 hybridized system, and in fact exhibit strong σ overlap with the surrounding C ligands. As such, we can create localized versions of these raMOs by taking linear combinations of the three functions (right). Six electrons would be needed to fill this Fe–C σ bonding system.

The three π-type raMOs also show significant contributions from the Fe and its C neighbors (Figure 7, middle). These

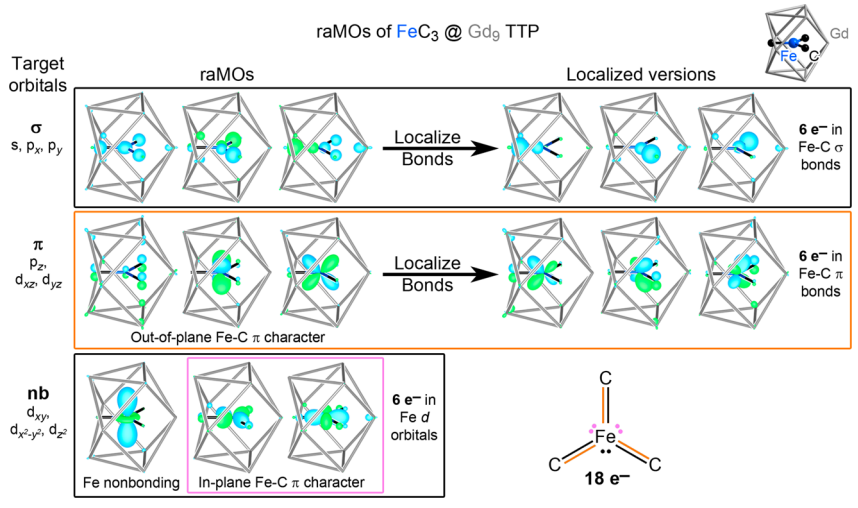

Figure 7. Results of raMO analysis on the FeC_3 @ Gd_9 fragment of $Gd_{13}Fe_{10}C_{13}$. Target orbitals are listed to the left of the raMOs to which they correspond. Each raMO represents an Fe–C bonding or Fe nonbonding orbital localized around the central Fe. These orbitals form an 18-electron configuration around the central Fe, allowing a Lewis structure to be drawn which shows three localized Fe–C σ and π bonds and three Fe lone pairs.

dx.doi.org/10.1021/ja505868w | J. Am. Chem. Soc. 2014, 136, 12073–12084

functions have substantial π overlap with ligand orbitals on the three surrounding C atoms. As in the σ system, we can create three localized Fe−C bonds from these raMOs. Six additional electrons are used by the phase to fill these Fe−C out-of-plane π bonding orbitals.

The raMO derived from the Fe d_{z^2} orbital (bottom panel, far left), has a very small amount of Fe−C σ character. However, as the majority of its density is pointed away from the C atoms, it can be treated simply as a lone pair of electrons on the Fe site.

The target orbitals for the final two raMOs, the Fe d_{xy} and $d_{x^2-y^2}$, lie in the FeC_3 plane and have nodal properties that are appropriate for σ interactions with some C neighbors and π interactions with others. Hybridization with the p_x and p_y could better separate these functions into pure σ and π sets, which would improve the σ character of the p-based functions and enhance the π character of the d-based functions. In terms of π overlap, clear Fe−C bonding is present in these raMOs. However, as we have only two functions but three Fe−C interactions, localized π bonds cannot be created here.

The role of these in-plane orbitals in π bonding can be seen in more detail by looking at how their raMOs spread out into the larger context of the structure, as seen for an Fe_4C_9 paddle wheel fragment in Figure 8. The orbitals here not only show

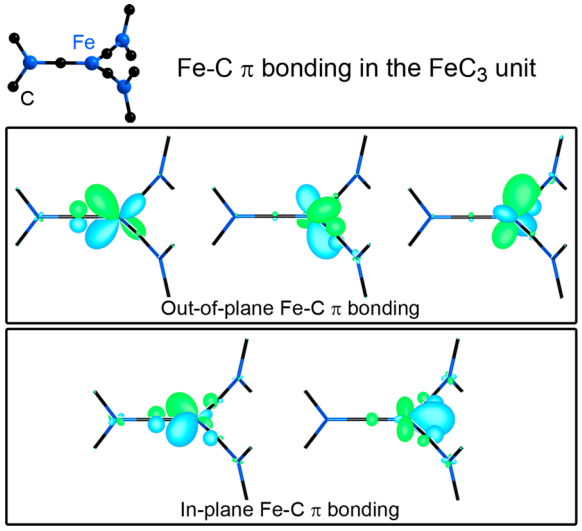

Figure 8. Conjugation in the Fe−C π interactions revealed through raMO analysis. A display of the raMOs over the larger context of an Fe center reveals that local π bonding corresponds to electron donation into the π^* orbitals of the Fe−C π interactions of the neighboring Fe atoms.

bonding character with the C p orbitals, but also interact with the π^* functions of the out-of-plane C−Fe interactions on the neighboring Fe atoms. The in-plane Fe−C π interactions thus occur via electron donation in the Fe−C π^* orbitals of the neighboring Fe. In other words, the in-plane electron pairs exhibit conjugation with the π bonding electron pairs centered on the next Fe atoms.[66] For book-keeping purposes, we will treat these in-plane orbitals as lone pairs on the Fe, while recognizing that they participate in π conjugation.

These results can be simply summarized in the form of a Lewis structure, as shown at the bottom right of Figure 7. The three localized Fe−C σ bonds, which account for 6 electrons on the Fe, are shown in black. The out-of-plane Fe−C π bonds, which can also be localized and account for 6 additional electrons on the Fe, are drawn in orange. The remainder of the electrons on the Fe site can be found in lone pairs. The lone pair shown in black represents 2 electrons in the Fe d_{z^2} orbital, while the two pink lone pairs represent 2 electrons each in the Fe d_{xy} and $d_{x^2-y^2}$ orbitals, with some π back-donation into C orbitals which we will examine in more detail below. In total, we arrive at the expected electron count of 6 (Fe−C σ) + 6 (Fe−C π) + 6 (Fe lone pairs) = 18 electrons on the central Fe.

3.5. raMO Analysis of the C_2FeFeC_2 Units. We are now ready to attempt a similar breakdown of the bonding on the more complex C_2FeFeC_2 sites. From the short distances between the Fe atoms in this unit, we should anticipate strong Fe−Fe interactions. Rather than trying to reproduce orbitals localized to individual atoms, then, a more productive route would be to consider orbitals for an Fe dimer. We thus considered symmetry adapted linear combinations (SALCs) of the Fe atomic orbitals as target functions.

Eighteen raMO functions result for the C_2FeFeC_2 cluster (Figure 9), most of which can be interpreted along the same lines as those of the FeC_3 unit. Four functions exhibit Fe−C σ bonding, and can be localized along the four Fe−C contacts by taking suitable linear combinations, as shown in Figure 9a. Six of the remaining functions correspond to in- or out-of-plane Fe−C π interactions (Figure 9b; more on these in the next section), and two are essentially Fe-centered lone pairs (Figure 9c). We can thus quickly account for 12 of the 18 raMOs.

The remaining six functions are deeply involved in Fe−Fe interactions, and might be expected to underlie the short distances of these contacts. The set of two orbitals in Figure 9d represent the Fe−Fe σ and σ^* functions for the fragment. The lower σ bonding function is generated from a combination of the Fe $d_{x^2-y^2}$ and p_x orbitals and has substantial Fe−Fe σ overlap. The upper function has some minor p character on the C atoms but no visible density on either Fe. As this raMO represents the best possible reconstruction of the combination of Fe orbitals in a σ antibonding fashion using only filled crystal orbitals, we can conclude that all Fe−Fe σ^* orbitals are empty. The net σ bond order between the Fe atoms is then 1.

Finally, as seen in Figure 9e, the last four raMOs involve Fe−Fe π overlap. The lower two raMOs have significant Fe−Fe π bonding character, while the two upper orbitals have corresponding Fe−Fe π antibonding character. However, the Fe−Fe π^* orbitals in these raMOs are hybridized outward, offsetting their Fe−Fe π^* character, while the Fe−Fe π orbitals are hybridized inward to maximize overlap. When combined with the observation that the orbital character on the Fe atoms is higher in the π than in the π^* function, it becomes clear that the antibonding character does not completely cancel out the Fe−Fe π bonding at these sites. We will therefore treat these two orbitals as partially occupied Fe−Fe π^* orbitals.

From this analysis of the Fe−Fe contacts (as well as complementary analyses using COHP and projected DOS curves of the raMOs; see the Supporting Information), we can conclude that some degree of net Fe−Fe π bonding is present. All three methods show two filled or mostly filled Fe−Fe π orbitals, as well as two partially filled π^* orbitals which lead to the cancellation of some, but not all, of the Fe−Fe π character. Since a full Fe−Fe σ bond is present, each Fe atom in the Fe_2C_4 unit contributes somewhat less than two electrons to bonding with its Fe neighbor: one electron in the σ system and roughly one electron in the π system. If we assume that these shared electrons bring the total electrons at each Fe to 18, we arrive at an electron count of 16 for each Fe in the Fe_2C_4 unit. The same

dx.doi.org/10.1021/ja505868w | J. Am. Chem. Soc. 2014, 136, 12073−12084

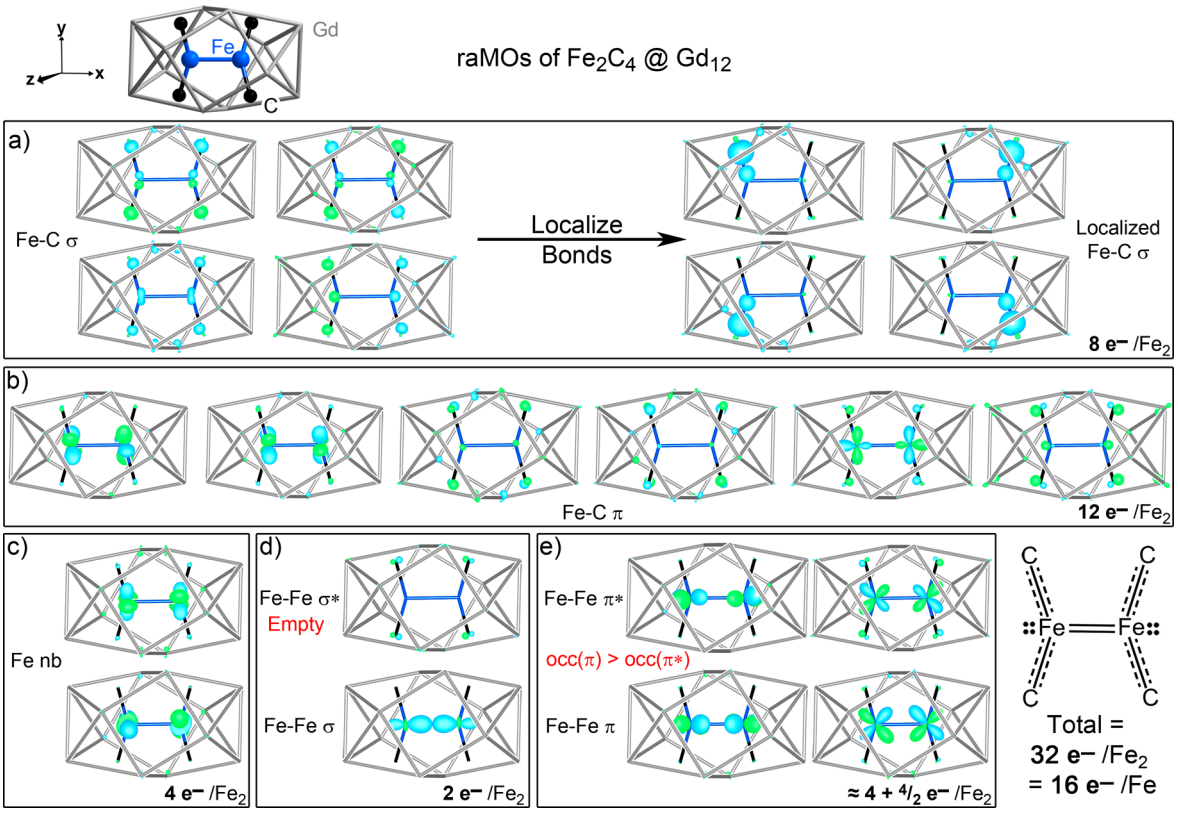

Figure 9. Results of raMO analysis on the Fe_2C_4 @ Gd_{12} fragment of $Gd_{13}Fe_{10}C_{13}$. Each raMO was constructed by combining the 9 orbitals on each of the two central Fe atoms, resulting in 18 total orbitals which represent Fe−C bonding, Fe−Fe bonding, or Fe nonbonding states localized around the Fe sites. Orbitals are classified by the type of bonding they exhibit, and empty or partially filled orbitals are labeled in red. Fifteen orbitals are filled, two are partially filled, and one is empty, giving a total of ∼16 electrons/Fe atom and supporting the presence of an Fe−Fe double bond.

number is obtained from populating the raMO functions of Figure 9 so that the σ^* orbital is empty and the π^* orbitals are half-filled.

3.6. Fe−C π Conjugation and the Allyl Anion. Our description of the Fe−C π interactions can be made clearer through an analogy to the π system observed for the molecular allyl anion $C_3H_5^-$. Two resonance Lewis structures for allyl are shown in Figure 10. These resonance structures show that a C−C π bond can be drawn between the middle carbon and either of the two end carbon atoms, with a lone pair on the other carbon site. The pair of resonance structures represent a prototypical 3 center-4 electron π bond from the donor−acceptor point of view.[67]

From a raMO analysis on the π system of this anion, we can see one representation of such a 3 center-4 electron interaction. We begin by considering the terminal orbitals as target states, which would correspond to the localized electron pairs in the resonance structures, and then perform a raMO analysis on this model system using the occupied MOs of the allyl anion as a basis set. The resulting raMO functions, shown in Figure 10a, exhibit familiar themes from our analysis of π bonding in $Gd_{13}Fe_{10}C_{13}$. For both raMO functions, the original p orbital of the target state is well reproduced, and participates in bonding overlap in a π fashion to the neighboring carbon, which is in turn antibonding with respect to the last carbon atom in the molecule. This corresponds to π donation from the target lone pair into the π^* orbital of the neighboring C−C π bond. The equal weights of the two resonance structures at the top of Figure 10 are reflected in the two raMOs generated from opposite ends of the molecule being mirror images of each other.

In Figure 10b,c, we show the corresponding raMO functions for the Fe−C−Fe units of $Gd_{13}Fe_{10}C_{13}$. The relative magnitudes of the features here are different from those of the allyl π system, but the nodal characteristics show close parallels. When we start with any of the π-oriented d orbitals on one of the Fe centers, a raMO is created that shows π donation from that orbital into the π^* orbital of the neighboring C−Fe contact. The Fe−C π systems thus appear as isolobal to those of the allyl π system, or to 3 center-4 electron interactions in general.

3.7. Role of Oxygen Substitution. Our overall theoretical picture of $Gd_{13}Fe_{10}C_{13}$ shows that stable 18-electron configurations are achieved on both types of Fe site through extensive Fe−C conjugated π bonds as well as partial Fe−Fe π bonding for the Fe_2C_4 site. A stable electron count is predicted to occur with a total of 18 electrons for each FeC_3 site and 16 electrons for each Fe in an Fe_2C_4 unit. As there are six Fe atoms per formula unit in FeC_3 sites and four Fe atoms per formula unit in Fe_2C_4 environments, we predict a total of $6 \times 18 + 4 \times 16 = 172$ electrons needed to give all Fe atoms an 18-electron configuration.

Since all Gd valence electrons are donated to the Fe−C bonding subsystem and no C−C bonding or C lone pairs that do not interact with the Fe atoms are present, 172 electrons would thus be expected to be equal to the total number of valence electrons per formula unit. If we compare this number to the total obtained from the stoichiometry, $(13 \times 3) + (10 \times 8) + (13 \times 4) = 171$ electrons per formula unit of $Gd_{13}Fe_{10}C_{13}$,

dx.doi.org/10.1021/ja505868w | J. Am. Chem. Soc. 2014, 136, 12073−12084

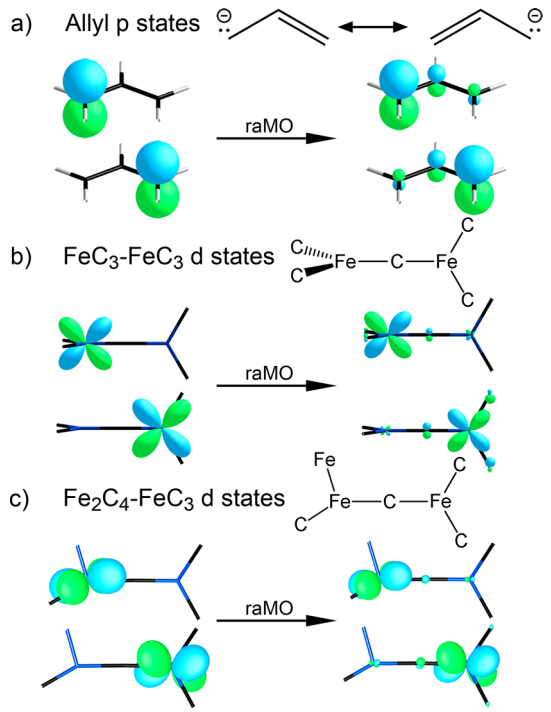

Figure 10. An isolobal analogy between the π systems of the allyl anion and Fe−C−Fe units in $Gd_{13}Fe_{10}C_{13}$. (a) The raMOs generated from either of the terminal π-oriented atomic orbitals in the allyl anion exhibit parallel nodal characteristics to those produced for the Fe−C−Fe units connecting (b) two FeC_3 units or (c) an Fe_2C_4 unit and an FeC_3 unit.

we see close agreement, but the phase falls short of fully satisfying the electronic requirements of all of its Fe sites by one electron per formula unit.

This observation suggests a possible explanation for the tendency of samples to form the oxycarbide $Gd_{13}Fe_{10}C_{13-x}O_x$ when exposed to O_2 before annealing. Oxygen has two more valence electrons than carbon, so a small degree of oxygen substitution would help satisfy the compound's slight electron deficiency. At an oxygen content of $x = 0.5$, an electron precise compound would be achieved. As $Gd_{13}Fe_{10}C_{13}$ and the orthorhombic stacking variant adopted by the oxycarbide exhibit nearly identical local geometries, this stabilization would be expected to apply for both structures, but for a still unknown reason leads to the orthorhombic structure being preferred.

4. CONCLUSIONS

In this Article, we have discussed the complex crystal structures and unusual bonding of two new carbometalates: $Gd_{13}Fe_{10}C_{13}$ and its oxygenated derivative $Gd_{13}Fe_{10}C_{13-x}O_x$. They crystallize in related structure types which feature Fe-centered Gd tricapped trigonal prisms encapsulated in an extended Fe−C network. This network is built from FeC_3 and Fe_2C_4 units, which interlock through shared C atoms and feature unusually short Fe−Fe and Fe−C bonds. We have used ^{57}Fe Mossbauer spectroscopy and raMO analysis in order to probe the bonding within this Fe−C network. The results reveal a complex network of Fe−Fe and Fe−C contacts connected through σ bonding and conjugated π systems. As we have seen with other intermetallics, this π bonding facilitates 18-electron configurations on the Fe sites in $Gd_{13}Fe_{10}C_{13}$. In addition, an isolobal analogy can be drawn between the π bonding in the linear Fe−C−Fe units, which are ubiquitous in $Gd_{13}Fe_{10}C_{13}$, and the 3 center-4 electron π bonding in the allyl anion. Intriguingly, our bonding analysis predicts that $Gd_{13}Fe_{10}C_{13}$ is slightly electron deficient, suggesting that the oxycarbide forms when samples are exposed to oxygen during synthesis in order to more fully achieve an ideal electron count.

Our original motivation for investigating the Gd−Fe−C system was the potential for chemical frustration between the differing geometrical preferences of the metal−metal and metal−carbon interactions. The crystal structures of $Gd_{13}Fe_{10}C_{13}$ and $Gd_{13}Fe_{10}C_{13-x}O_x$ show vividly the way in which this system copes with frustration. The structures are built from frameworks of Fe-centered Gd tricapped trigonal prisms similar to those found in the common intermetallic structure type Fe_2P. Carbon atoms then insert themselves into this framework at interstices that can easily be deformed into the octahedral geometries preferred by C in carbides. The relative electronegativities of Gd < Fe < C lead to a charge transfer from the Gd to the Fe−C sublattice and the formation of strong covalent bonds along Fe−C and Fe−Fe contacts. The extensive π bonding in this network, and the corresponding isolobal analogy to the allyl anion, provides deeper connections between bonding in intermetallics and organic molecules that are especially important for the broad family of carbometalates and related carbides, whose TM−C bonding networks have often been compared to organometallics.[36]

The difficulty of analyzing localized bonding in inorganic solid state structures has historically been a barrier to fully analyzing the bonding in many carbometalates. raMO analysis offers a means of determining electron counts for TM sites in carbometalates without assigning arbitrary oxidation states to the TM atoms, and provides an orbital-based view which can be used to determine the σ and π character of individual bonds. We are eager to apply this method to other carbometalates and more complex carbides in order to extend the bonding principles outlined here.

Of course, the issue of interpreting the electronic structures of large and complex chemical systems in terms of simple bonding schemes is not limited to carbometalates. The capabilities of the raMO approach demonstrated here for $Gd_{13}Fe_{10}C_{13}$ should also be applicable to the far broader range of systems in which the bonding at a region of interest must be discerned in the wave functions of the full system. Examples include the metal clusters stabilized by bulky ligands, or even metal-containing cofactors in proteins. Along these lines, we are excited that this theoretical tool, which was developed originally for understanding intermetallics in molecular terms, may in turn be used to elucidate bonding problems in molecular systems.

■ ASSOCIATED CONTENT

Supporting Information

Experimental procedures for incorporating O_2 into samples. Additional powder X-ray diffraction data and experimental procedures for synchrotron powder diffraction measurements. Crystallographic data tables for $Gd_{13}Fe_{10}C_{13-x}O_x$. Mössbauer spectra and spectral parameters. Hückel parameters used for electronic structure calculations on $Gd_{13}Fe_{10}C_{13}$ and the allyl anion. This material is available free of charge via the Internet at http://pubs.acs.org.

dx.doi.org/10.1021/ja505868w | J. Am. Chem. Soc. 2014, 136, 12073−12084

AUTHOR INFORMATION

Corresponding Author

danny@chem.wisc.edu

Notes

The authors declare no competing financial interest.

ACKNOWLEDGMENTS

We thank Dr. Chris Ceccarelli at Agilent Technologies for collecting a data set on $Gd_{13}Fe_{10}C_{13-x}O_x$ using an Agilent SuperNova A diffractometer. We thank Prof. John Berry for useful discussions about metal−metal and metal−carbon bonding and Mössbauer spectroscopy. Prof. Huifang Xu and Dr. John Fournelle of the UW-Madison Department of Geoscience provided assistance with the powder X-ray diffraction measurements on the Rigaku Rapid II instrument and the SEM/EDS measurements, respectively. Use of the Advanced Photon Source at Argonne National Laboratory was supported by the U.S. Department of Energy, Office of Science, Office of Basic Energy Sciences, under Contract No. DE-AC02-06CH11357. We gratefully acknowledge financial support from the Department of Energy Office of Science Early Career Research Program (DE-SC0003947), through the Office of Basic Energy Sciences.

REFERENCES

(1) Bodak, O. I.; Marusin, E. P.; Bruskov, V. A. *Kristallografiya* **1980**, *25*, 617−619.
(2) Gerss, M. H.; Jeitschko, W. *Z. Naturforsch., B: Chem. Sci.* **1986**, *41*, 946−950.
(3) Behrens, R. K.; Jeitschko, W. *Monatsh. Chem.* **1987**, *118*, 43−50.
(4) Gueramian, M.; Bezinge, A.; Yvon, K.; Muller, J. *Solid State Commun.* **1987**, *64*, 639−644.
(5) Helmholdt, R. B.; Buschow, K. H. J. *J. Less-Common Met.* **1989**, *155*, 15−21.
(6) Aksel'rud, L. G.; Bodak, O. I.; Marusin, E. P.; Aslan, A. M. *Kristallografiya* **1990**, *35*, 487−490.
(7) Khalili, M. M.; Bodak, O. I.; Marusin, E. P.; Pecharskaya, A. O. *Kristallografiya* **1990**, *35*, 1378−1380.
(8) Kahnert, G. E.; Jeitschko, W. *Z. Anorg. Allg. Chem.* **1993**, *619*, 93−97.
(9) Pöttgen, R.; Block, G.; Jeitschko, W.; Behrens, R. K. *Z. Naturforsch., B: Chem. Sci.* **1994**, *49*, 1081−1088.
(10) Dashjav, E.; Kreiner, G.; Schnelle, W.; Wagner, F. R.; Kniep, R.; Jeitschko, W. *J. Solid State Chem.* **2007**, *180*, 636−653.
(11) Dashjav, E.; Prots, Y.; Kreiner, G.; Schnelle, W.; Wagner, F. R.; Kniep, R. *J. Solid State Chem.* **2008**, *181*, 3121−3130.
(12) Benbow, E. M.; Dalal, N. S.; Latturner, S. E. *J. Am. Chem. Soc.* **2009**, *131*, 3349−3354.
(13) Gerss, M. H.; Jeitschko, W.; Boonk, L.; Nientiedt, J.; Grobe, J.; Morsen, E.; Leson, A. *J. Solid State Chem.* **1987**, *70*, 19−28.
(14) Demooij, D. B.; Buschow, K. H. J. *J. Less-Common Met.* **1988**, *142*, 349−357.
(15) Sun, H.; Hu, B. P.; Li, H. S.; Coey, J. M. D. *Solid State Commun.* **1990**, *74*, 727−730.
(16) Lee, W. H.; Zeng, H. K.; Yao, Y. D.; Chen, Y. Y. *Physica C* **1996**, *266*, 138−142.
(17) Gerdes, M. H.; Jeitschko, W.; Wachtmann, K. H.; Danebrock, M. E. *J. Mater. Chem.* **1997**, *7*, 2427−2431.
(18) Reehuis, M.; Gerdes, M.; Jeitschko, W.; Ouladdiaf, B.; Stusser, T. *J. Magn. Magn. Mater.* **1999**, *195*, 657−666.
(19) Hillier, A. D.; Quintanilla, J.; Cywinski, R. *Phys. Rev. Lett.* **2009**, *102*, 117007.
(20) Scherer, W.; Hauf, C.; Presnitz, M.; Scheidt, E. W.; Eickerling, G.; Eyert, V.; Hoffmann, R. D.; Rodewald, U. C.; Hammerschmidt, A.; Vogt, C.; Pöttgen, R. *Angew. Chem., Int. Ed.* **2010**, *49*, 1578−1582.
(21) Tucker, P. C.; Lita, A.; Latturner, S. E. *Chem. Mater.* **2013**, *25*, 1480−1482.
(22) Jeitschko, W.; Gerss, M. H.; Hoffmann, R. D.; Lee, S. *J. Less-Common Met.* **1989**, *156*, 397−412.
(23) Harris, N. A.; Hadler, A. B.; Fredrickson, D. C. *Z. Anorg. Allg. Chem.* **2011**, *637*, 1961−1974.
(24) Hadler, A. B.; Fredrickson, D. C. *J. Am. Chem. Soc.* **2012**, *134*, 10361−10364.
(25) Endter, F.; Klemm, W. *Z. Anorg. Allg. Chem.* **1950**, *252*, 377−377.
(26) Spedding, F. H.; Gschneidner, K.; Daane, A. H. *J. Am. Chem. Soc.* **1958**, *80*, 4499−4503.
(27) Yvon, K.; Parthé, E. *Acta Crystallogr., Sect. B* **1970**, *26*, 149−153.
(28) Yvon, K.; Parthé, E. *Acta Crystallogr., Sect. B* **1970**, *26*, 153−163.
(29) Hendricks, S. B.; Kosting, P. R. *Z. Kristallogr.* **1930**, *74*, 511−533.
(30) Fredrickson, R. T.; Fredrickson, D. C. *Inorg. Chem.* **2012**, *51*, 10341−10349.
(31) Fredrickson, R. T.; Fredrickson, D. C. *Inorg. Chem.* **2013**, *52*, 3178−3189.
(32) Yannello, V. J.; Kilduff, B. J.; Fredrickson, D. C. *Inorg. Chem.* **2014**, *53*, 2730−2741.
(33) Dashjav, E.; Kreiner, G.; Schnelle, W.; Wagner, F. R.; Kniep, R. *Z. Anorg. Allg. Chem.* **2004**, *630*, 689−696.
(34) Jeitschko, W.; Block, G.; Kahnert, G. E.; Behrens, R. K. *J. Solid State Chem.* **1990**, *89*, 191−201.
(35) Hoffmann, R. D.; Wachtmann, K. H.; Ebel, T.; Jeitschko, W. *J. Solid State Chem.* **1995**, *118*, 158−162.
(36) King, R. B. *J. Organomet. Chem.* **1997**, *536*, 7−15.
(37) Jeitschko, W.; Behrens, R. K. *Z. Metallkd.* **1986**, *77*, 788−793.
(38) Dashjav, E.; Schnelle, W.; Kreiner, G.; Kniep, R. *Z. Kristallogr.−New Cryst. Struct* **2005**, *220*, 129−130.
(39) Hoffmann, R.; Li, J.; Wheeler, R. A. *J. Am. Chem. Soc.* **1987**, *109*, 6600−6602.
(40) Lee, S.; Jeitschko, W.; Hoffmann, R. D. *Inorg. Chem.* **1989**, *28*, 4094−4104.
(41) Deng, H.; Hoffmann, R. *Inorg. Chem.* **1993**, *32*, 1991−1996.
(42) King, R. B. *J. Indian Chem. Soc.* **2000**, *77*, 603−607.
(43) Miller, G. J. *Chem. Soc. Rev.* **2006**, *35*, 799−813.
(44) *CrysAlisPro Software System*, Version 171.36.24; Agilent Technologies: Yarnton, UK, 2010.
(45) Oszlányi, G.; Sütő, A. *Acta Crystallogr., Sect. A* **2004**, *60*, 134−141.
(46) Oszlányi, G.; Sütő, A. *Acta Crystallogr., Sect. A* **2005**, *61*, 147−152.
(47) Palatinus, L.; Chapuis, G. *J. Appl. Crystallogr.* **2007**, *40*, 786−790.
(48) Petříček, V.; Dušek, M.; Palatinus, L. *Jana2006. The Crystallographic Computing System*; Institute of Physics: Praha, Czech Republic, 2006.
(49) Iwata, T.; Kaga, M.; Nakano, H.; Fukuda, K. *J. Solid State Chem.* **2009**, *182*, 2252−2260.
(50) Kaga, M.; Iwata, T.; Nakano, H.; Fukuda, K. *J. Solid State Chem.* **2010**, *183*, 636−642.
(51) Kaga, M.; Urushihara, D.; Iwata, T.; Sugiura, K.; Nakano, H.; Fukuda, K. *J. Solid State Chem.* **2010**, *183*, 2183−2189.
(52) Flack, H. D. *Acta Crystallogr., Sect. A* **1983**, *39*, 876−881.
(53) Stacey, T. E.; Fredrickson, D. C. *Dalton Trans.* **2012**, *41*, 7801−7813.
(54) Landrum, G. A.; Glassy, W. YAeHMOP: Yet Another extended Hückel Molecular Orbital Package, Version 3; YAeHMOP is freely available at http://sourceforge.net/projects/yaehmop/.
(55) Dronskowski, R.; Blöchl, P. E. *J. Phys. Chem.* **1993**, *97*, 8617−8624.
(56) Stadelmaier, H. H.; Park, H. K. *Z. Metallkd.* **1981**, *72*, 417−422.
(57) Fredrickson, D. C.; Doverbratt, I.; Ponou, S.; Lidin, S. *Crystals* **2013**, *3*, 504−516.
(58) Greenwood, N. N.; Earnshaw, A. *Chemistry of the Elements*; 2nd ed.; Butterworth-Heinemann: Oxford, 1997.

(59) Hanson, A. W. *Acta Crystallogr.* **1962**, *15*, 930−933.
(60) Dickson, D. P. E.; Berry, F. J. *Mössbauer Spectroscopy*; Cambridge University Press: Cambridge, 1986.
(61) Van der Kraan, A. M.; Buschow, K. H. J. *Physica B, C* **1986**, *138*, 55−62.
(62) Chelvane, J. A.; Markandeyulu, G.; Raja, M. M. *Hyperfine Interact.* **2008**, *184*, 27−31.
(63) In some Fe oxides and coordination complexes, a negative isomer shift has been correlated with rare iron(V) or (VI) oxidation states. See Guenzberger, D.; Esquivel, D. M. S.; Danon, J. *Phys. Rev. B* **1978**, *18*, 4561−4569. However, such a positive oxidation state seems unlikely for $Gd_{13}Fe_{10}C_{13}$.
(64) Long, G. J.; Kulasekere, R.; Pringle, O. A.; Grandjean, F.; Buschow, K. H. J. *J. Magn. Magn. Mater.* **1992**, *117*, 239−250.
(65) Zaikina, J. V.; Schellenberg, I.; Benbow, E. M.; Pöttgen, R.; Latturner, S. E. *Chem. Mater.* **2011**, *23*, 1768−1778.
(66) This examination of how the raMOs of one Fe atom spill out onto other Fe atoms is important in terms of electron counting. The raMO functions generated for the valence orbitals of one Fe atom are guaranteed to be orthogonal to each other, but are not necessarily orthogonal to those generated in separate raMO analyses of other Fe sites. However, in this conjugation over Fe−C−Fe contacts, we witness a bonding function on the central Fe atom spreading into an antibonding function that would appear as unoccupied in the raMO analysis of the second Fe atom. As this antibonding character would not be perceived in the raMO analysis of the second Fe atom, the raMOs of the two Fe centers can be confirmed as being linearly independent. No overcounting of electrons is then expected to result from treating these Fe centers with raMO analysis separately.
(67) Weinhold, F.; Landis, C. R. *Valency and Bonding: A Natural Bond Orbital Donor-Acceptor Perspective*; Cambridge University Press: Cambridge, U.K.; New York, 2005.